

PAPER • OPEN ACCESS

## Doublet splitting of fusion alpha particle driven ion cyclotron emission

To cite this article: J W S Cook 2022 *Plasma Phys. Control. Fusion* **64** 115002

View the [article online](#) for updates and enhancements.

You may also like

- [Comparing theory and simulation of ion cyclotron emission from energetic ion populations with spherical shell and ring-beam distributions in velocity-space](#)  
B Chapman, R O Dendy, S C Chapman et al.

- [Interpretation of suprathermal emission at deuteron cyclotron harmonics from deuterium plasmas heated by neutral beam injection in the KSTAR tokamak](#)  
B. Chapman, R.O. Dendy, S.C. Chapman et al.

- [Chirping ion cyclotron emission \(ICE\) on NSTX-U](#)  
E.D. Fredrickson, N.N. Gorelenkov, R.E. Bell et al.

# Doublet splitting of fusion alpha particle driven ion cyclotron emission

J W S Cook<sup></sup>

UKAEA-CCFE, Culham Science Centre, OX14 3DB Abingdon, United Kingdom

E-mail: [james.cook@ukaea.uk](mailto:james.cook@ukaea.uk)

Received 25 May 2022, revised 28 July 2022

Accepted for publication 22 August 2022

Published 20 September 2022



## Abstract

Ion cyclotron emission (ICE) originating from confined populations of fast ions in toroidal fusion plasmas is an important non-invasive, passive diagnostic for current and next-generation devices. The ability to model ICE signals accurately is an essential step towards inferring the characteristics of confined energetic alpha particles or fast neutral beam ions and background plasma. In this paper, the linear growth rates of the magnetoacoustic cyclotron instability, which is the leading explanation for ICE, are calculated in high-resolution 2D ( $k_{\perp}, k_{\parallel}$ ) space for parameters corresponding to JET Pulse No. 26148. These calculations further highlight the origin of doublet splitting of the cyclotron harmonics and the perceived need to invoke nonlinear interactions with 1D3V particle-in-cell studies to account for lower harmonics with substantial amplitudes. The inclusion of signals of ICE from a well-resolved range of propagation angles can also account for these effects.

Keywords: ion cyclotron emission, magnetoacoustic cyclotron instability, JET, doublet splitting

(Some figures may appear in colour only in the online journal)

## 1. Introduction

Observations of ion cyclotron emission (ICE) have been reported from magnetically confined plasmas first in TFTR [1, 2] and JET [2–4], followed by other tokamaks PDX [5], JT-60-U [6], DIII-D [7], ASDEX [8], KSTAR [9, 10], ASDEX-Upgrade [11], TUMAN-3 M [12], NSTX and NSTX-U [13], and EAST [14]. Stellarators [15] and field-reversed configurations [16] have also exhibited this phenomenon. Energetic ion populations that generate ICE have their origins in fusion reactions in DT plasmas [1, 17], ion cyclotron resonance heating [17] and neutral beam injection [11]. The ICE arising from fusion alpha particles is a proposed route to further the understanding of burning plasmas in ITER [18, 19].

The foremost explanation of the mechanism responsible for ICE is the magnetoacoustic cyclotron instability (MCI) [20],

which arises from the free energy present in energetic ions with inverted distributions in the velocity space. The theoretical understanding of ICE is based on analytical solutions to the linearised Maxwell–Vlasov system of equations [21], where the energetic ion species is modelled as a ring-beam for which  $f(v_{\parallel}, v_{\perp}) \propto \exp(-(v_{\parallel} - u_{\parallel})^2/v_{\text{th}}^2)\delta(v_{\perp} - u_{\perp})$  [22, 23]. Here  $u_{\parallel}$ ,  $u_{\perp}$  and  $v_{\text{th}}$  are the beam velocity (the signed drift speed along the magnetic field), the ring speed (the speed of the shifted centre of the inverted population perpendicular to the magnetic field) and the thermal velocity, respectively. Subsequent studies augmented this understanding via nonlinear fully kinetic [9, 24] and hybrid [25, 26] particle-in-cell (PIC) simulations in one spatial dimension with three vector components for velocities and electromagnetic field (i.e. 1D3V), and recently in 2D3V hybrid-PIC simulations [27]. These computational approaches operate under similar simplifications as the analytical treatments in that the plasma is initially spatially homogeneous and periodic in the spatial domain. Linearised fluid approaches that incorporate toroidal geometry along with inhomogeneous plasma and magnetic fields have highlighted the eigenmode structure of compressional Alfvén eigenmodes, which as with ICE, are also fast Alfvén modes



Original Content from this work may be used under the terms of the [Creative Commons Attribution 4.0 licence](#). Any further distribution of this work must maintain attribution to the author(s) and the title of the work, journal citation and DOI.

driven by energetic ions in spherical tokamaks [28, 29] and conventional aspect ratio tokamaks [30–32].

The effectiveness of the linear theory to reproduce the observed cyclotron harmonic peaks in the fluctuations of the magnetic field was first explained somewhat by 1D PIC simulations [24]. In these simulations the onset of nonlinearity appeared to imprint the amplitudes of each of the harmonics into the signal as they are at the end of the linear phase. Each mode grows independently until growth is terminated for all modes when the fastest mode enters its nonlinear phase, meaning that both the amount of free energy available for instability has decreased and the unstable ion distribution function has been perturbed into a more stable state. A previous analysis showed that only higher cyclotron harmonics are destabilised [19] to the MCI under these particular conditions; however, experimental observations clearly indicate power at theoretically stable lower harmonics [3]. In a further step towards the accurate recreation of experimental observations, nonlinear phases of hybrid [25] and fully kinetic [9, 24] PIC simulations went on to show that wave–wave coupling is responsible for raising the amplitude of lower cyclotron harmonics. Most recently, hybrid 2D simulations have begun to shed light on the 2D3V dynamics of ICE [27].

Fine detailed structure has been observed in ICE spectra, such as the doublet splitting of individual harmonics on JET [4] and DIII-D [33] and even multiplet splitting on TUMAN-3M [12], ASDEX-Upgrade [34] and EAST [14], which has been made possible by advances in the resolution of diagnostic techniques. This paper highlights an underlying kinetic mechanism that produces doublet splitting because of Doppler-shifted resonances and the intricate landscape of the MCI growth rate on the fast Alfvén dispersion surface in  $(k_\perp, k_\parallel)$  space. In principle, splitting could be produced by grad-B or curvature drifts [4, 35] or potentially any mechanism that can add a Doppler shift to the wave-particle resonance condition. Note that this study focusses on edge ICE, which is named for the region of plasma from which the signal arises, as opposed to the core ICE [11, 14].

To better enable ICE as a diagnostic for confined fast ions, it is necessary to further develop our understanding with a wide range of tools. This work presents the growth rates in 2D wavenumber space of the MCI under the conditions of the outer mid-plane of the JET PTE [4] Pulse No. 26148. These growth rates are obtained from a dispersion relation solver, LinearMaxwellVlasov.jl [36], written in the Julia programming language [37]. These results narrow the gap between the analytical theory and expensive high-performance computing simulations and can be run on desktop computers in a matter of minutes, further enabling research into this topic.

In section 2, the computational method is described for calculating the linear growth rates of the MCI, which are presented for energetic ring-beam alpha particles with non-zero perpendicular thermal spread in section 3 where a comparison is made to the observations on JET. The results are summarised in section 4.

## 2. Computational method

Solutions to the linearised Maxwell–Vlasov system of equations are found in perpendicular and parallel wavenumber space,  $(k_\perp, k_\parallel)$ , for a ring-beam distribution of energetic minority alpha particles, Maxwellian electrons and Maxwellian majority deuteron ions. The ring-beam distribution function, equation (1), is a separable function of the beam in  $v_\parallel$  given by equation (2) and the ring in  $v_\perp$  given by equation (3). In the context of the fully kinetic Maxwell–Vlasov linear theory, which rests upon the assumption of an infinite homogeneous plasma and a straight uniform magnetic field, this distribution function is parameterised by the drift velocity parallel to the magnetic field  $u_\parallel$ , the shift of the Maxwellian distribution perpendicular to the magnetic field  $u_\perp$ , and the isotropic thermal velocity  $v_{\text{th}}$ . The thermal spread of the alpha particles' distribution function is  $v_{\text{th}} = v_{\parallel,\text{th}} = v_{\perp,\text{th}} = u_0/100$ . The number density ratio of alpha particles to the majority fuel deuterons is  $1.5 \times 10^{-4}$ .

$$f_\alpha(v_\parallel, v_\perp) = f_{\alpha,\parallel}(v_\parallel) f_{\alpha,\perp}(v_\perp) \quad (1)$$

$$f_{\alpha,\parallel}(v_\parallel) = \frac{\exp\left(-\frac{(v_\parallel - u_\parallel)^2}{v_{\parallel,\text{th}}^2}\right)}{v_{\parallel,\text{th}} \sqrt{2\pi}} \quad (2)$$

$$f_{\alpha,\perp}(v_\perp) = \frac{\exp\left(-\frac{(v_\perp - u_\perp)^2}{v_{\perp,\text{th}}^2}\right)}{\frac{1}{2\pi} \left( \frac{\sqrt{\pi}}{2} v_{\perp,\text{th}} u_\perp (1 - \text{erf}(-\frac{u_\perp}{v_{\perp,\text{th}}})) + \exp(-u_\perp^2/v_{\perp,\text{th}}^2) \frac{v_{\perp,\text{th}}^2}{2} \right)}. \quad (3)$$

Calculations are made for alpha particles with ring beams of two values of the pitch angle cosine:  $u_\parallel = -0.646 u_0 \approx -\cos(\arcsin(\sqrt{R_0 \sin(\psi_0)/R_{\text{ICE}}}) u_0) \simeq -1.1 V_A$ , which is associated with the ICE observed on JET Pulse No. 26148 for which  $R_0 = 3.46$  m and  $\psi_0 = 55.2^\circ$  are the major radius and pitch angle at birth, respectively, and  $R_{\text{ICE}} = 4$  m is the major radius of the emission region: see figures 3 and 14 and associated text in [4]; and  $(u_\parallel = 0 u_0, u_\perp = u_0)$  representing a ring distribution with no parallel drift, see figure 1(a) of [24]. Here,  $V_A$  is the Alfvén speed and  $u_0 = \sqrt{u_\parallel^2 + u_\perp^2}$  is the speed of an alpha particle with an energy of 3.6 MeV.

The plasma parameters approximate those found at the outer mid-plane edge ( $R = 4$  m,  $Z = 0$  m), where the electrons and deuterons have temperatures of 1 keV and the electrons have a number density of  $1.7 \times 10^{19} \text{ m}^{-3}$ . The magnetic field is 2.07 T at this major radius.

Although curvature and grad-B drift terms would be present in fast alpha particle populations on JET and these drifts would alter the wave-particle resonance condition, it is worth noting that they are both of the order of the ratio of the Larmor radius

to the machine size,  $\rho^*$ , and have been neglected in these calculations where  $u_\perp \gg \rho^* u_0$  is always the case.

Solutions to the linearised Maxwell–Vlasov system of equations are given by the dispersion relation, equation (4), which is satisfied for sets of  $(\omega, k)$  along the fast Alfvén branch on a grid of  $(k_\perp, k_\parallel)$ .

$$0 = |\vec{\epsilon} + (\vec{k} \otimes \vec{k} - \vec{I}(\vec{k} \cdot \vec{k})) \frac{c^2}{\omega^2}|, \quad (4)$$

The hot dielectric tensor [21]  $\vec{\epsilon}$ , given by equation (5), is calculated for each species,  $s$ ,

$$\vec{\epsilon} = \vec{1} + \sum_s \frac{\Pi_s^2}{\omega} \sum_{n=-\infty}^{\infty} \int_0^\infty \int_{-\infty}^\infty \frac{\vec{S}_{s,n} 2\pi v_\perp dv_\perp dv_\parallel}{\omega - k_\parallel v_\parallel - n\Omega_s} \quad (5)$$

where

$$\vec{S}_{s,n} = \begin{bmatrix} \frac{n^2 J_n^2}{z_s^2} v_\perp U_s & \frac{i n J_n J'_n}{z_s} v_\perp U_s & \frac{n J_n^2}{z_s} v_\perp W_{s,n} \\ -\frac{i n J_n J'_n}{z_s} v_\perp U_s & (J'_n)^2 v_\perp U_s & -i J_n J'_n v_\perp W_{s,n} \\ \frac{n J_n^2}{z_s} v_\parallel U_s & i J_n J'_n v_\parallel U_s & n J_n^2 v_\parallel W_{s,n} \end{bmatrix}, \quad (6)$$

$$U_s = \frac{\partial f_s}{\partial v_\perp} + \frac{k_\parallel}{\omega} \left( v_\perp \frac{\partial f_s}{\partial v_\parallel} - v_\parallel \frac{\partial f_s}{\partial v_\perp} \right), \quad (7)$$

$$W_{s,n} = \left( 1 - \frac{n\Omega_s}{\omega} \right) \frac{\partial f_s}{\partial v_\parallel} + \frac{n\Omega v_\parallel}{\omega v_\perp} \frac{\partial f_s}{\partial v_\perp}. \quad (8)$$

$J_n$  is the  $n$ th Bessel function of the first kind taking the argument  $z_s = k_\perp v_\perp / \Omega_s$  and  $J'_n = \frac{\partial J_n}{\partial z}$ .

Integrals over perpendicular velocity required for calculating the dielectric tensor for Maxwellian distribution functions are given in terms of modified Bessel functions of the first kind [21] for both electrons and deuterons, i.e. when  $u_\perp = 0$ . The same perpendicular integrals over the alpha particles' ring distribution given by equation (3) are calculated numerically via Gauss–Kronrod [38] quadrature using the GaussGK.jl [39] library. An absolute and relative tolerance of 0 and  $10^{-8}$ , respectively, is used to confirm the convergence of the integral values. Since all the parallel distribution functions for all species are Maxwellian, the parallel integrals can be calculated from the well-known plasma dispersion function [40], which is presented in the appendix.

The Bessel function indices,  $n$ , in equation (5) are incremented outwards from 0 in both the positive and negative directions until the relative change between the current summand and that of the previous iteration is less than a tolerance of  $10^{-8}$ . The root finding of equation (4) in the complex frequency plane for a given  $(k_\perp, k_\parallel)$ -pair is performed by an amalgamation of the Nelder–Mead [41] optimisation method with the winding number method. If the complex values at the nodes of the Nelder–Mead simplex, which in this case is just a triangle, have a winding number of 0 and therefore the simplex does not contain a root, then the optimisation procedure follows the Nelder–Mead method, otherwise the simplex bifurcates. The child simplex that contains

the root is used for the next iteration. The optimisation iteration procedure finishes successfully when the simplex that encircles a root is small enough such that its extent in the real (imaginary) frequency is less than  $10^{-4} \Omega_i$  ( $10^{-5} \Omega_i$ ), where  $\Omega_i$  is the cyclotron frequency of both the alpha particles and deuterons because they share a charge–mass ratio. This approach is found to be adequately robust and faster than either the Nelder–Mead method or the winding number approach used separately. Each  $512 \times 512$  scan in  $(k_\perp, k_\parallel)$  takes between 5 and 6 min on a current laptop.

### 3. Linear growth rates

The growth rates of unstable modes for the case where the pitch angle cosine value is 0 ( $u_\parallel = 0$  in equation (1)) are plotted in figure 1(a) against the associated real frequency (only modes with growth rates in excess of the solver tolerance are shown, i.e.  $\Im(\omega) > 10^{-5} \Omega_i$ ). In this panel, shading indicates parallel wavenumber in units of  $\Omega_i/V_A$ . Figure 1(b) plots the same data in the  $(\omega, k_\parallel)$  plane where the shading instead indicates growth rate in units of  $\Omega_i$ . The simplicity of the consecutive unstable cyclotron harmonics visible in panel (a) betrays the complexity of the structure in the  $(\omega, k_\parallel)$  plane. The integration over  $k_\parallel$  projects the solutions onto the frequency axis, which loses the structure and produces narrow harmonics. Figure 2 depicts a  $(k_\perp, k_\parallel)$  space view of the same data as figure 1 as well as damped and normal modes, except that shading indicates the growth rate. The overlaid contours indicate the real frequency in units of ion cyclotron harmonics. Only narrow regions around the cyclotron harmonics are unstable. The overlaid straight traces show the propagation angle. No Doppler shift is present due to the lack of parallel drift in the alpha particle ring beam. The growth rate increases approximately linearly with cyclotron harmonic number, which is consistent with the literature [22]. Together, these figures serve to introduce a 2D view (growth rates in  $(k_\perp, k_\parallel)$  space) of the traditionally 1D data (growth rates against frequency). The importance of a non-zero  $u_\parallel$  is discussed next.

Figure 3 plots solutions for the physically more realistic pitch case ( $u_\parallel = -0.646 u_0$ ) in the same manner as figure 1, except there is an additional black trace in the upper panel that represents the measured JET ICE intensity signal; the continuous trace from figure 2 in [4]. These observations of ICE intensity are plotted on a log scale that is scaled to match the range of the linear MCI growth rates. A direct comparison of log-scale ICE observations and linear growth rates is justified to the extent that nonlinear PIC simulations indicate that the linearly unstable modes rising as  $\exp(\gamma t)$ , where  $\gamma$  is a mode's growth rate, cease to grow once the fastest growing mode becomes nonlinear [24]. Therefore, under the assumption that all modes start growing in unison from identical seed amplitudes, the log of a mode's amplitude is proportional to its growth rate. Although this simplification neglects possibly important effects, such as particle sink and source terms and their influence on the nonlinear amplitudes of the observed ICE signals, it is still possible to obtain important information regarding the signals' structure and overall trends.

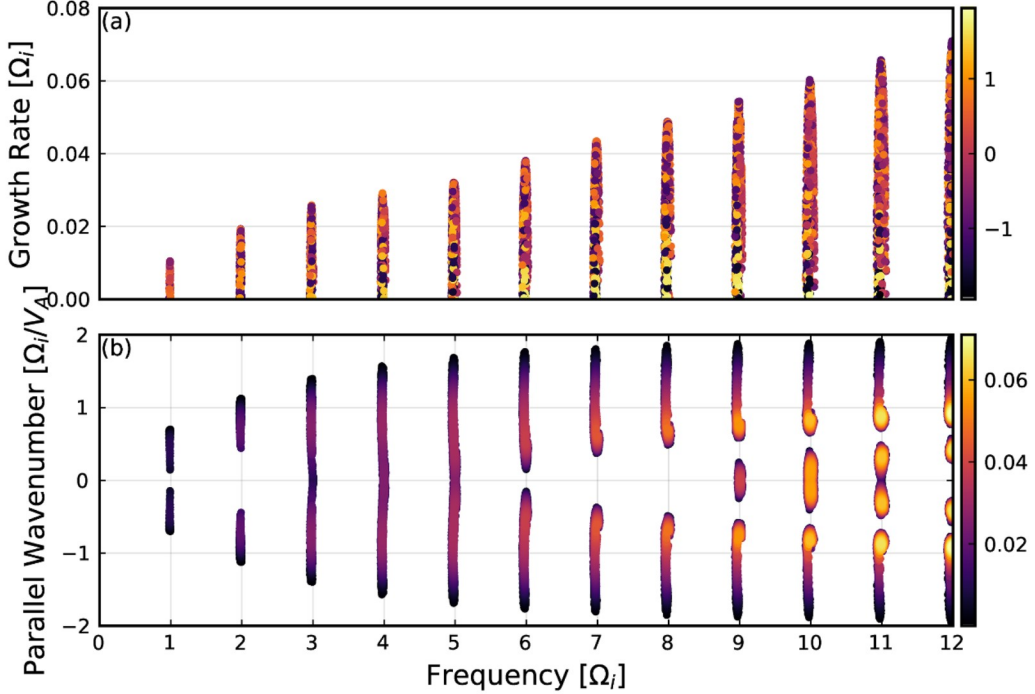


**Figure 1.** Unstable fast Alfvén wave solutions to the linear Maxwell–Vlasov system of equations, equation (4), for thermal electrons, deuterons and a ring distribution of energetic alpha particles, i.e. when there is zero parallel drift,  $u_{\parallel} = 0$  in equation (1). (a) Upper panel: growth rate as a function of real frequency where shading indicates the parallel wavenumber,  $k_{\parallel}$ , in units of  $\Omega_i/V_A$  of the complex frequency solution. Consecutive cyclotron harmonics are increasingly unstable and are narrow due to the lack of Doppler shift associated with parallel drifts. (b) Lower panel: the same solutions as in panel (a) in the  $(\omega, k_{\parallel})$  plane where shading indicates the growth rate in units of  $\Omega_i$ . The complex structure of the growth rates that exists in the wavenumber space is projected into sharp harmonics on the frequency axis.

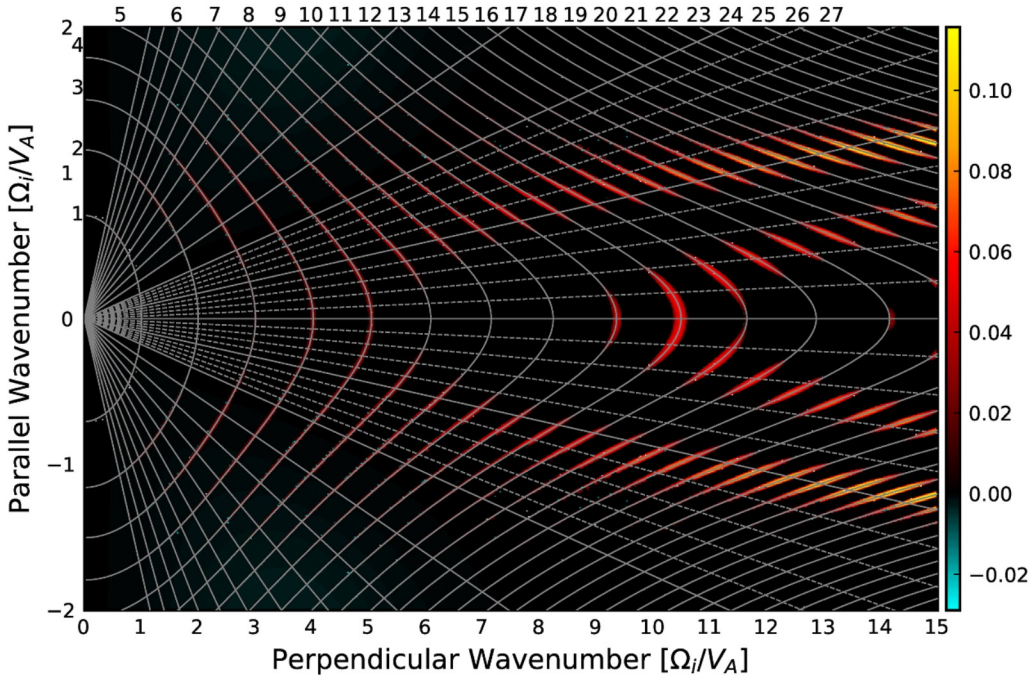


**Figure 2.** Shading indicates the growth rate of fast Alfvén waves excited by a ring of fusion-born alpha particles, as a function of parallel wavenumber on the ordinate and perpendicular wavenumber on the abscissa. No solution is found where shading is absent. The alpha particle distribution function is given by equation (1) with  $u_{\parallel} = 0$ . Consecutive straight traces indicate propagation angle with respect to the magnetic field: the horizontal line is exactly perpendicular; solid traces fan out at intervals of five degrees; and dashed traces indicate intervals of one degree. Curved grey traces indicate the location in  $(k_{\perp}, k_{\parallel})$  of the cyclotron harmonics (i.e. the real component of the complex  $\omega$  solutions), which are annotated along the left-hand side and upper edge of the figure. Frequencies are in units of the alpha particle cyclotron frequency, and wavenumbers are in the alpha particle cyclotron frequencies per Alfvén speed. Note that the up-down symmetry is due to the lack of parallel drift in the energetic alpha particles.

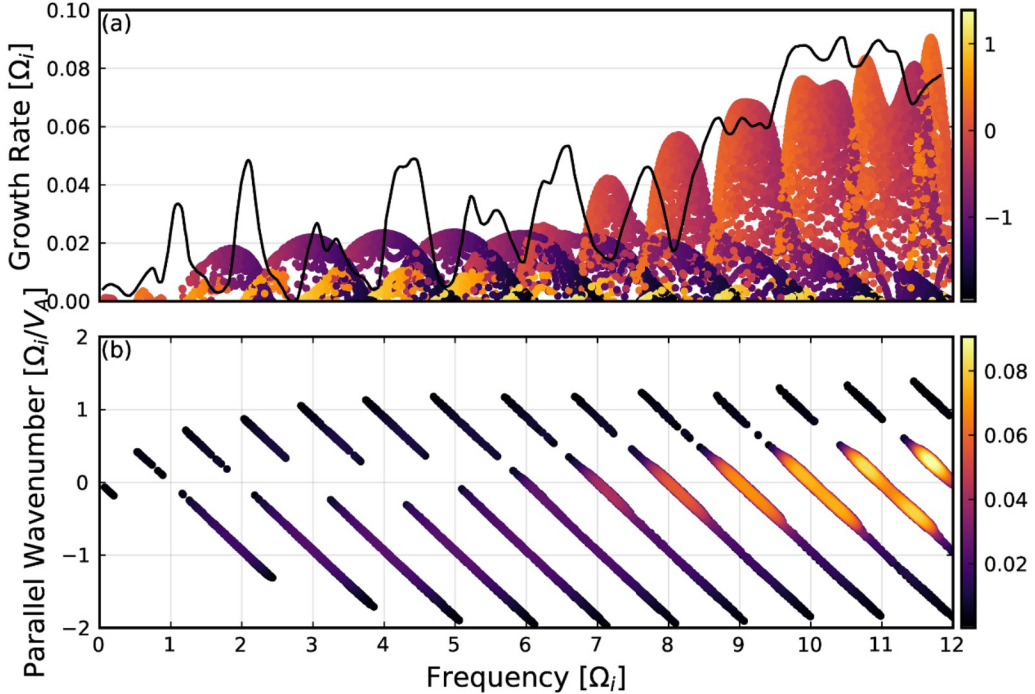


**Figure 3.** As in figure 1, except for the case with the parallel drift:  $u_{\parallel} = -0.646 u_0 \simeq -1.1 V_A$ . (a) Upper panel: growth rate against frequency where shading indicates the parallel wavenumber in units of  $\Omega_i/V_A$  and the black trace shows the re-scaled ICE signal from JET Pulse #26148 digitised from figure 2 of Cottrell *et al* [4] (with permission from IOP Publishing). Reproduced courtesy of the IAEA. Figure from [4]. Copyright (1993) the IAEA. (b) Lower panel: solutions in the  $(\omega, k_{\parallel})$  plane where shading indicates growth rate. Note that the Doppler shift associated with the non-zero parallel drift speed broadens the unstable peaks in frequency. The 10th and 11th cyclotron harmonics are split into doublets, i.e. they have two peaks.

Several points are worth noting about figure 3. First, the growth rate is no longer linear with cyclotron harmonic number. Second, harmonics are broader due to the non-zero parallel drift that gives rise to a strong Doppler shift with increasing  $|k_{\parallel}|$ . Third, the doublet splitting of the 10th and 11th harmonics is observed; see figure 2 of [4] for a single signal showing multiple doublet splittings. The following describes how these three features are connected. Doublet splitting arises because of the dip in the growth rate along the band of instability where  $k_{\parallel}$  goes through zero combined with the change in sign of the Doppler shift of the real frequency as  $k_{\parallel}$  changes sign, which pushes the real frequency from one side of the harmonic to the other. The effect is larger for higher harmonics where the growth rate diminishes to zero for perpendicular propagation. This is hinted at by figure 3 of [22] (also figure 9 [2]), which shows growth rates at slices of the propagation angle that when all superimposed point towards doublet splitting, albeit under-resolved in the wavenumber space.

Doublet splitting can be seen in figure 4, which is the counterpart to figure 3 as figure 2 is to figure 1, at, e.g. the 12th harmonic near  $(k_{\parallel} \simeq 0 \Omega_i/V_A, k_{\perp} \simeq 13 \Omega_i/V_A)$ . Qualitatively, the outline of the scattered points in figure 3(a) resembles the experimental observations given by the black trace in that the signal below the seventh cyclotron harmonic is lower and flatter with well-defined peaks and the signal beyond the seventh harmonic is a step-change larger and the harmonics

are less easily identifiable. These features cannot be recreated with a 1D calculation for these distribution functions since they arise from contributions from a range of propagation angles. Figure 4 shows these two different regimes more clearly. The lower frequency behaviour, where  $k_{\perp} < 7 \Omega_i/V_A$ , is characterised by narrow regions of instability near Doppler-shifted cyclotron harmonics that are stable when  $k_{\parallel} = 0$  and unstable at larger negative parallel wavenumbers. The higher frequency behaviour in the region  $k_{\perp} \geq 7 \Omega_i/V_A$  is dominated by broader bands of instability near Doppler-shifted cyclotron harmonics, which have an intricate structure in wavenumber space. Modes numbering 1–5 and 14 are stable when propagating exactly perpendicular whilst obliquely propagating modes remain unstable. The magnitude of the Doppler shift of the growing modes can reach  $\approx \Omega_i$  for large propagation angles at lower frequencies and also for oblique angles at higher frequencies; see, for example, the mode associated with the 15th cyclotron harmonic near  $k_{\parallel} \simeq -\frac{3}{4} \Omega_i/V_A, k_{\perp} \simeq 13 \Omega_i/V_A$ , i.e. a propagation angle of  $\sim 93^\circ$ . Furthermore, the breadth of the harmonics can be attributed to the contributions from multiple propagation angles even though the lower harmonics are largely stable for forward travelling modes and propagation angles that are close to perpendicular.

Figure 5 shows the smoothed real frequency part of the solution, as depicted by contours on figures 2 and 4, for the case of zero pitch-angle cosine and is normalised by the

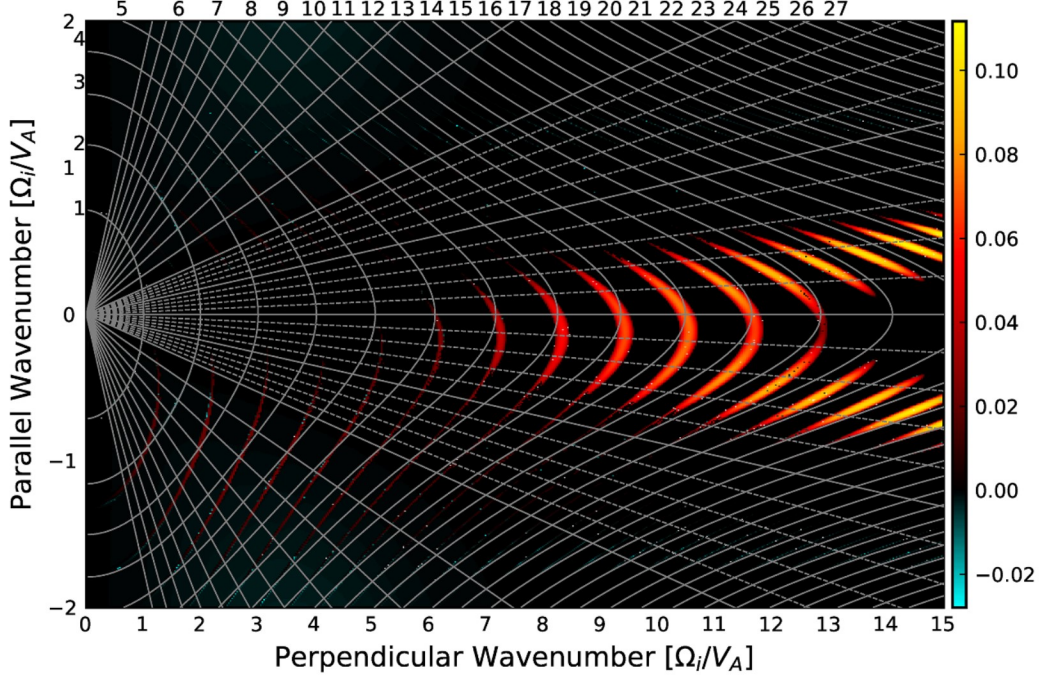


**Figure 4.** As shown in figure 2, except for a ring beam of alpha particles with a more realistic pitch angle value  $u_{\parallel} = -0.646 u_0 \simeq -1.1 V_A$ . The non-zero parallel drift speed causes up-down asymmetry; this figure for a pitch-angle cosine of the opposite sign,  $u_{\parallel} = 0.646 u_0$ , is identical except flipped about  $k_{\parallel} = 0$ .

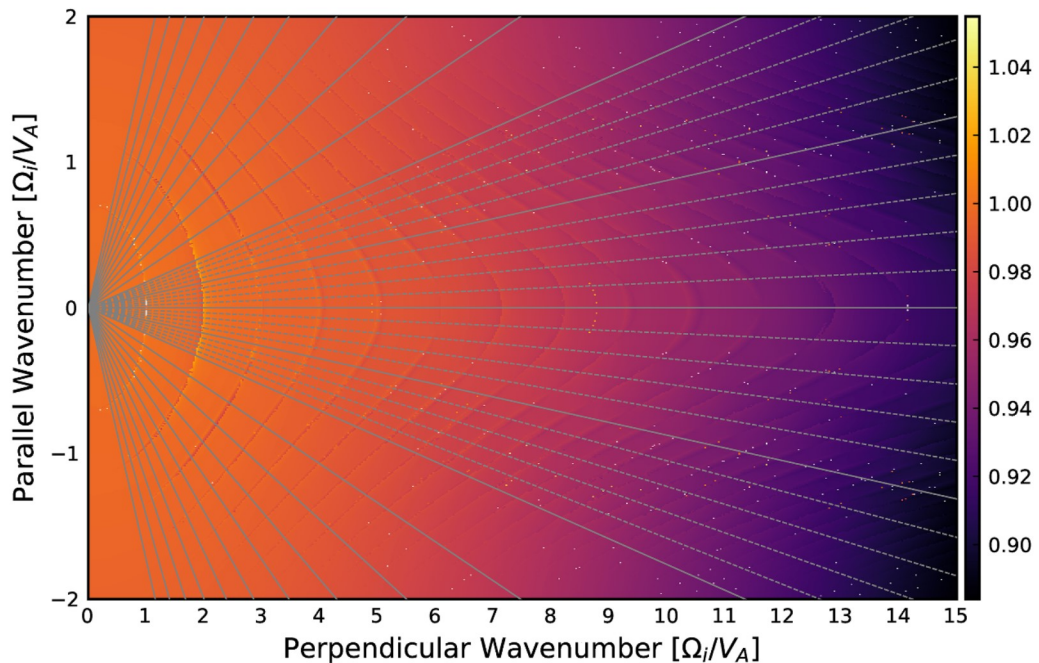


**Figure 5.** As in figure 2, except that shading indicates the real part of the smoothed solution normalised by the high-frequency expression for the fast Alfvén wave set out in equation (9) (equation (25) of [22], which is also equation (11) in [23]). The differences in real frequencies for the two sets of calculations, a pitch angle cosine of  $-0.646$  and zero, are negligible.

high-frequency expression for the fast Alfvén wave set out in equation (25) of [22] (also equation (11) of [23]),

$$\omega^2 = \frac{V_A^2}{2} \left[ k^2 + k_{\parallel}^2 + k^2 k_{\parallel}^2 \frac{V_A^2}{\Omega_i^2} \right. \\ \left. + \sqrt{\left( k^2 + k_{\parallel}^2 + k^2 k_{\parallel}^2 \frac{V_A^2}{\Omega_i^2} \right)^2 - 4k^2 k_{\parallel}^2} \right], \quad (9)$$

where  $k^2 = k_{\parallel}^2 + k_{\perp}^2$ . No discernable difference is present for the non-zero pitch case.

#### 4. Summary

This paper presents the linear Maxwell–Vlasov dispersion relationship of a plasma comprising thermal electrons, thermal deuteron fuel ions and a minority energetic ring-beam of fusion-born alpha particles. These high-resolution ( $k_{\perp}, k_{\parallel}$ ) calculations revisit ICE observations from JET Pulse No. 26148 [2, 4] and reproduce several important features: the step change in signal strength from  $\omega < 7 \Omega_i$  to  $\omega \geq 7 \Omega_i$ ; the doublet splitting of peaks at  $\omega \approx 10 \Omega_i$  in figure 3, with origins visible in the fine ( $k_{\perp}, k_{\parallel}$ ) structure in figure 4. The Doppler shift for large  $k_{\parallel}$  is comparable in magnitude to the alpha particle cyclotron frequency making it difficult to determine which parts of the signal come from which cyclotron harmonic numbers. This outcome has important implications for determining the major radius of origin of ICE. Further research is required to account for the extra doublets visible in the continuous trace associated with JET Pulse No. 26148 in figure 2 of [4].

These calculations capture the finite perpendicular thermal spread of the alpha particle distribution function, the integral of which has no known analytically tractable form. The computational capabilities of the software, LinearMaxwellVlasov.jl, used to generate the results further enable ICE as a diagnostic for fusion plasmas since the code is capable of calculating the dispersion relation of plasmas consisting of an arbitrary number of species and of arbitrary distribution functions, although those with parallel Maxwellians, like those presented here, are handled faster. It has been shown that it is possible to qualitatively recreate signals containing lower harmonics of substantial amplitudes by invoking 2D linear physics. The presence of ICE signals at lower harmonics in PIC simulations has been attributed to nonlinear interactions between the pairs of more powerful higher harmonics [25]. This work suggests that observations of lower ICE harmonics may arise because of 2D linear physics effects, but does not exclude the possibility that nonlinear 1D physics [10] may also play a part.

Several important features are missing from these calculations. Among them are the drifts and other effects associated with the spatial inhomogeneity of the magnetic field and the background plasma, and quantisation arising from toroidal periodicity. These effects may create an eigenmode structure, not accounted for herein, associated with the kinetic

MCI. Cottrell *et al* [4] discussed the implications of propagation angles on ICE signals and indicated that lower harmonics must propagate increasingly close to exactly perpendicular. It remains the subject of further work to incorporate these effects into linear and nonlinear studies of ICE.

This work showcases a new high-resolution tool for studying ICE and captures some of the fine details of ICE signals, which are challenging to capture with nonlinear PIC code simulations because they suffer from low resolution in frequency and wavenumber space due to the phenomenon's transience and computational expense, respectively. As such, this work represents a complementary tool that builds upon purely analytical and nonlinear PIC studies to provide an explanation of doublet splitting, which in turn enhances the feasibility of exploiting ICE as a passive diagnostic of confined and leaving ions in magnetised fusion plasmas.

#### Data availability statement

The data that support the findings of this study are openly available at the following URL/DOI: DOI: [10.5281/zenodo.705162](https://doi.org/10.5281/zenodo.705162).

#### Acknowledgments

It is a pleasure to thank R O Dendy and B Chapman-Olopouli for useful discussions.

#### Appendix

The plasma dispersion function [40]

$$Z_n(z) = \frac{1}{\sqrt{\pi}} \int_{-\infty}^{\infty} \frac{x^n e^{-x^2}}{x - z} dx, \quad (A.1)$$

can be calculated via the recurrence relation [42]

$$Z_n(z) = z Z_{n-1}(z) + \begin{cases} 0 & \text{if } n \in \{2k : k \in \mathbb{Z}\} \\ 1 & \text{if } n = 1 \\ \frac{1}{2} & \text{if } n = 3 \\ 2^{\frac{1-n}{2}} \prod_{i=1}^{\frac{n-3}{2}} (2i+1) & \text{otherwise,} \end{cases} \quad (A.2)$$

where  $n \geq 0$  and the cases  $n = 1$  and  $n = 3$  are stated explicitly to avoid confusion. The zeroth term is defined as

$$Z_0(z) = i\sqrt{\pi} \operatorname{erfcx}(-iz) \quad (A.3)$$

where  $\operatorname{erfcx}$  is the scaled complementary complex error function.

#### ORCID iD

J W S Cook  <https://orcid.org/0000-0002-1905-5218>

## References

- [1] Cauffman S, Majeski R, McClements K G and Dendy R O 1995 *Nucl. Fusion* **35** 1597
- [2] Dendy R O *et al* 1995 *Nucl. Fusion* **35** 1733–42
- [3] Cottrell G A and Dendy R O 1988 *Phys. Rev. Lett.* **60** 33–36
- [4] Cottrell G A *et al* 1993 *Nucl. Fusion* **33** 31365–87
- [5] Heidbrink W and Sadler G 1994 *Nucl. Fusion* **34** 535–615
- [6] Ichimura M, Higaki H, Kakimoto S, Yamaguchi Y, Nemoto K, Katano M, Ishikawa M, Moriyama S and Suzuki T 2008 *Nucl. Fusion* **48** 035012
- [7] Heidbrink W W *et al* 2011 *Plasma Phys. Control. Fusion* **53** 085028
- [8] D'Inca R 2014 Ion cyclotron emission on ASDEX Upgrade *PhD Thesis* Ludwig-Maximilians-Universität
- [9] Chapman B, Dendy R O, McClements K G, Chapman S C, Yun G S, Thatipamula S G and Kim M H 2017 *Nucl. Fusion* **57** 124004
- [10] Chapman B, Dendy R O, Chapman S C, McClements K G, Yun G S, Thatipamula S G and Kim M H 2018 *Nucl. Fusion* **58** 096027
- [11] Ochoukov R *et al* 2018 *Rev. Sci. Instrum.* **89** 10J101
- [12] Askinazi L G *et al* 2018 *Nucl. Fusion* **58** 082003
- [13] Fredrickson E D, Gorelenkov N N, Bell R E, Diallo A, LeBlanc B P and Podestá M 2019 *Phys. Plasmas* **26** 032111
- [14] Liu L *et al* 2020 *Nucl. Fusion* **60** 044002
- [15] Saito K *et al* 2013 *Plasma Sci. Technol.* **15** 209–12
- [16] Nicks B S, Magee R, Necas A and Tajima T 2021 *Nucl. Fusion* **61** 016004
- [17] Cottrell G A 2000 *Phys. Rev. Lett.* **84** 2397–400
- [18] Dendy R O and McClements K G 2015 *Plasma Phys. Control. Fusion* **57** 044002
- [19] McClements K G and Dendy R O 2015 *Nucl. Fusion* **55** 043013
- [20] Belikov V S and Kolesnichenko Y I 1976 *Sov. Phys. Tech. Phys.* **20** 1146
- [21] Stix T H 1992 *Waves in Plasmas* 2nd edn (New York: Springer)
- [22] Dendy R O, Lashmore-Davies C N, McClements K G and Cottrell G A 1994 *Phys. Plasmas* **1** 1918–28
- [23] McClements K G , Dendy R O, Lashmore-Davies C N, Cottrell G A, Cauffman S and Majeski R 1996 *Phys. Plasmas* **3** 543
- [24] Cook J W S, Dendy R O and Chapman S C 2013 *Plasma Phys. Control. Fusion* **55** 065003
- [25] Carbajal L, Dendy R O, Chapman S C and Cook J W S 2014 *Phys. Plasmas* **21** 012106
- [26] Reman B *et al* 2019 *Nucl. Fusion* **59** 096013
- [27] Carbajal L and Calderón F A 2021 *Phys. Plasmas* **28** 014505
- [28] Sharapov S E, Lilley M K, Akers R, Ayed N B, Ceccanello M, Cook J W S, Cunningham G and Verwichte E 2014 *Phys. Plasmas* **21** 082501
- [29] Gorelenkov N N 2016 *New J. Phys.* **18** 105010
- [30] Kolesnichenko Y I, Fülöp T, Lisak M and Anderson D 1998 *Nucl. Fusion* **38** 1871
- [31] Fülöp T, Lisak M, Kolesnichenko Y I and Anderson D 2000 *Phys. Plasmas* **7** 1479–86
- [32] Heidbrink W W *et al* 2006 *Nucl. Fusion* **46** 324
- [33] Thome K E, Pace D C, Pinsker R I, Meneghini O, del Castillo C A and Zhu Y 2018 *Rev. Sci. Instrum.* **89** 10I102
- [34] Ochoukov R *et al* 2019 *Nucl. Fusion* **59** 086032
- [35] Fülöp T and Lisak M 1998 *Nucl. Fusion* **38** 761
- [36] Cook J W S 2022 *LinearMaxwellVlasov.jl* (0.1.0) (Zenodo) (<https://doi.org/10.5281/zenodo.6529288>)
- [37] Bezanson J, Edelman A, Karpinski S and Shah V B 2017 *SIAM Rev.* **59** 1
- [38] Kronrod A S 1965 *Nodes and Weights of Quadrature Formulas. Sixteen-Place Tables* (New York: Consultants Bureau (Authorized translation from the Russian))
- [39] Johnson S G 2022 QuadGK.jl: Gauss-Kronrod integration in Julia (available at: <https://github.com/JuliaMath/QuadGK.jl>)
- [40] Fried B D and Conte S C 1961 *The Plasma Dispersion Function* (New York: Academic)
- [41] Nelder J A and Mead R 1965 *Comput. J.* **7** 4
- [42] Sampoorna M, Nagendraa K N and Frisch H 2007 *J. Quant. Spectrosc. Radiat. Transfer* **104** 71–85

